Effect of soil surface roughness and scene components on soil surface bidirectional reflectance factor

Z. Wang[1], C. A. Coburn[2], X. Ren[1], and P. M. Teillet[1]

[1]Department of Physics and Astronomy, University of Lethbridge, 4401 University Drive West, Lethbridge, Alberta, Canada T1K 3M4; and [2]Department of Geography, University of Lethbridge, 4401 University Drive West, Lethbridge, Alberta, Canada T1K 3M4. Received 5 July 2011, accepted 12 December 2011.

Wang, Z., Coburn, C. A., Ren, X. and Teillet, P. M. 2012. **Effect of soil surface roughness and scene components on soil surface BRF**. Can. J. Soil Sci. **92**: 297–313. Bidirectional Reflectance factor (BRF) data of both rough [surface roughness index (SRI) of 51%] and smooth soil surfaces (SRI of 5%) were acquired in the laboratory under 30° illumination zenith angle using a Specim V10E imaging spectrometer and an Ocean Optics non-imaging spectrometer mounted on the University of Lethbridge Goniometer System version 2.5 (ULGS-2.5) and version 2.0 (ULGS-2.0), respectively. Under controlled laboratory conditions, the rough soil surface exhibited higher spectral reflectance than the smooth surface for most viewing angles. The BRF of the rough surface varied more than the smooth surface as a function of the viewing zenith angle. The shadowing effect was stronger for the rough surface than for the smooth surface and was stronger in the forward-scattering direction than in the backscattering direction. The pattern of the BRF generated with the non-image based data was similar to that generated with the whole region of interest (ROI) of the image-based data, and that of the whole ROI of the image-based data was similar to that of the illuminated scene component. The BRF of the smooth soil surface was dominated by illuminated scene component, i.e., the sunlit pixels, whereas the shaded scene component, i.e., the shaded pixels, was a larger proportion of the BRF of the rough soil surface. The image-based approach allowed the characterization of the contribution of spatial components in the field of view to soil BRF and improved our understanding of soil reflectance.

Key words: Bidirectional reflectance factor, goniometer, soil reflectance, remote sensing

Wang, Z., Coburn, C. A., Ren, X. et Teillet, P. M. 2012. **Effets de la rugosité de la surface du sol et des composantes de la scène sur le FRB de la surface du sol**. Can. J. Soil Sci. **92**: 297–313. Des données du facteur de réflectivité bidirectionnelle (FRB) des surfaces rugueuses [index de rugosité de la surface (IRS) de 51%] et lisses (IRS de 5%) de sols nus ont été acquises dans le laboratoire sous un angle zénithale d'illumination de 30° utilisant un spectromètre imageur Specim V10E et un spectromètre non-imageur Ocean Optics montés sur les systèmes goniométriques de l'Université de Lethbridge versions 2.5 (ULGS-2.5) et 2.0 (ULGS-2.0), respectivement. Sous conditions contrôlées dans le laboratoire, la surface rugueuse a montré une réflectivité spectrale plus élevée que la surface lisse pour la plupart des angles de visée. Le FRB de la surface rugueuse a varié plus que celui de la surface lisse en fonction d'angle zénithale de visée. L'effet d'ombrage était plus fort pour la surface rugueuse que pour la surface lisse et était plus fort dans la direction de dispersion vers l'avant que dans la direction de rétrodiffusion. Le modèle du FRB généré à partir des données non-image était semblable à celui généré pour la région d'intérêt (RDI) entière des données image, et celui de la RDI entière des données image était semblable à celui des composantes illuminées de la scène. Le FRB de la surface de sol lisse a été dominé par les composantes illuminées de la scène, c.-à-d. les pixels directement ensoleillés, tandis que les composantes ombragées de la scène, c.-à-d. les pixels ombragés, correspondaient à une plus grande proportion du FRB de la surface de sol rugueuse. L'approche basée sur les image a permis la caractérisation de la contribution des composantes spatiales dans le champ de vue au FRB du sol et l'amélioration de notre compréhension de la réflectivité de sol.

Mots clés: Facteur de réflectivité bidirectionnelle (FRB), goniomètre, réflectivité du sol, télédétection

An improved understanding of the effect of imaging geometry on remotely sensed data is essential to improve our ability to interpret satellite data. Most Earth surfaces generate spectral reflectance signatures that are anisotropic with respect to view and illumination angles. This phenomenon can be described by the bidirectional reflectance distribution function (BRDF). The BRDF of a particular target represents the reflectance at all possible illumination and sensor view angles (Nicodemus et al. 1977). BRDF is defined as the ratio of the radiance L (W m^{-2} sr^{-1} μm^{-1}) reflected in an outgoing direction (θ_v, φ_v) to the incident irradiance

Abbreviations: **ASD**, analytical spectral devices; **BRDF**, bidirectional reflectance distribution function; **BRF**, bidirectional reflectance factor; **CV**, coefficient of variation; **CQI**, Czekanowski's quantitative index; **DC**, digital count; **FIGOS**, field goniometer system; **FOV**, field of view; **IS**, imaging spectrometer; **LPP**, light principal plane; **OO**, Ocean Optics; **PP**, perpendicular plane; **ROI**, region of interest; **SD**, standard deviation; **SFG**, Sandmeier field goniometer; **SRI**, surface roughness index; **2D**, two-dimensional; **ULGS**, University of Lethbridge goniometer system

E (W m^{-2} μm^{-1}) from a specific direction (θ_i, φ_i) (Nicodemus et al. 1977). The mathematical expression of BRDF is showing in Eq. 1.

$$BRDF = \frac{L(\theta_v, \phi_v)}{E(\theta_i, \phi_i)} \quad (1)$$

Where θ_v and ϕ_v are viewing zenith and azimuth angles, respectively, θ_i and ϕ_i and are the zenith and azimuth angles of the irradiance, respectively. As BRDF is a characteristic of reflectance referring to a monodirectional illumination at all possible angles of collection, it is impossible to measure under natural conditions (Nicodemus et al. 1977; Cierniewski and Courault 1993; Barnsley et al. 1994). However, the BRDF of natural surfaces can be estimated by means of the bidirectional reflectance factor (BRF), which is defined as the radiance reflected by the surface to the radiance which would be reflected by a perfect Lambertian panel (See Eq. 2), both under the same illumination and viewing conditions (Nicodemus et al. 1977).

$$BRF(\theta_i, \phi_i; \theta_v, \phi_v) = \frac{L_t(\theta_i, \phi_i; \theta_v, \phi_v)}{L_p(\theta_i, \phi_i; \theta_v, \phi_v)} \quad (2)$$

Where L_t is the radiance reflected by a target surface and L_p is the radiance reflected by a perfect Lambertian panel.

Remote sensing technologies have been applied to soil research for decades (Schmugge et al. 1974; Cierniewski 1987; Schmugge and Jackson 1994; Selige and Schmidhalter 2001; Ben-Dor et al. 2002; Chang and Laird 2002; Ladoni et al. 2010). Some studies have demonstrated that spectroscopy is capable of accurately determining soil organic carbon contents (Chang and Laird 2002; Ladoni et al. 2010), soil surface moisture (Schmugge et al. 1974; Schmugge and Jackson 1994), soil salinity (Ben-Dor et al. 2002) and soil nitrogen status (Selige and Schmidhalter 2001). While these studies have demonstrated that spectral data can provide important information over constrained spatial areas, larger spatial extents are difficult to accurately characterize due to the inherent complexity of natural soil surfaces. Natural soil surfaces are spatially complex and heterogeneous which causes variability in the spectral reflectance data used to derive information products (Oh and Kay 1998). BRDF in remote sensing usually is based on a model because a set of measurements over the full range of incident and reflected angles is practical only for laboratory instruments, and therefore is not appropriate for natural, structured surface because they are neither uniform nor isotropic (Snyder 2002). Effects observed in the laboratory may not necessarily be valid at the broader scale of remote sensing devices, and physically based BRDF models are often too complex to be inverted with remote sensing data or do not account for the heterogeneity of natural surfaces (Sandmeier and Strahler 2000). Soil roughness has also been noted as a significant limiting variable to the implementation of theoretical and numerical models of soil spectral reflectance or scattering as the models are based on rough soil surfaces rather than natural soil surfaces (Oh et al. 1992). However, Cierniewski (1987) developed a mathematical model dealing with the influence of soil surface roughness on soil reflectance and demonstrated that the simulated reflectance using this model fit the measured soil reflectance under natural environment conditions very well.

Soil spectral reflectance anisotropy is dependent on soil roughness and soil moisture factors. The measurement of soil BRF is, therefore, related to these two physical properties as well as a variety of other biochemical soil factors including soil organic matter, mineral content and soluble salts. Soil roughness has the greatest effect on the magnitude of the spectral reflectance anisotropy as the individual soil clods cast shadows and have facets that, due to their geometry, create a more pronounced hot spot effect. The influence of soil moisture is more pronounced in the short wave infrared and can cause spectral reflectance anisotropy due to its spatial heterogeneity (Ni and Li 2000). In general, the higher the organic matter content, the lower the reflectance of soils (Cierniewski and Kuśnierek 2010). Soil structure affects soil spectral reflectance by changing the direction of reflected radiance and trapping irradiance (Cierniewski and Kuśnierek 2010). Variation of the illumination angle plays a major role on the reflectance of rough surfaces as the individual soil clods cast shadows (Richter et al. 2005). Natural light is composed of a direct as well as a diffuse component scattered by the atmosphere and the surroundings of the observed target (Schaepman-Strub et al. 2005). Compared with the artificial light source, natural light always results in a considerable shape distortion of the BRF in the visible and near-infrared when no correction for the diffuse part of the illumination is performed, even under clear sky conditions (Lyapustin and Privette 1999).

Barnsley et al. (2000) reported that spatial variations in field measurements of broadband albedo are related to the fractional ground cover of different scene elements (live and senescent vegetation, soil and shadow). It was also shown that the separability of land cover types may be improved when using multiangular image data (Barnsley et al. 1997). To understand the factors controlling this spatial variation, the relative proportions of different scene elements need to be determined. Imaging spectroscopy is capable of generating qualitative and quantitative spatial indicators for ecologists, land managers, pedologists, and engineers (Ben-Dor et al. 2009). Cierniewski et al. (2010) used a Specim hyperspectral camera to collect soil BRF data and concluded that the variation in soil surface illumination conditions affects the soil spectral reflectance features of the illuminated points and the shaded soil fragments. With imaging spectrometer (IS) and multiangular image data, we can

see and better understand what the non-imaging systems are unable to see, and the target components that drive the soil BRF can be more fully studied.

Goniometer systems are preferred to sample BRF data as they accurately position the sensor over the target at different viewing zenith and azimuth angles through a rotatable arc and a sled on the arc. However, these systems are seldom used because they are expensive to build and cumbersome to use (Coburn and Peddle 2006). The well-known goniometer systems are FIGOS (FIeld GOniometer System) developed by the Remote Sensing Lab of the University of Zürich (Sandmeier and Itten 1999) and Sandmeier Field Goniometer (SFG), which was constructed by the NASA Ames Research Center based upon the FIGOS design. Both these systems have viewing resolution of 15° and 30° in zenith and azimuth directions, respectively. The FIGOS-style instruments' half-circle arc can easily cast shadows on the sample when the arc is positioned in (or close to) the light incident angles (Strub et al. 2002) and its base is apt to damage or disturb the target when operating this system in field conditions.

Vegetation canopies and soils often exhibit a pronounced peak in reflectance in the backscattering direction, known as the hot spot, where the angle between the illumination and the view direction (phase angle) tends to zero (Suits 1972; Hapke et al. 1996). Regardless of goniometer system design, data from this region are impossible to acquire and shadowing caused by the goniometer should be minimized to maintain information potential of the backscatter region.

Recently, Biliouris et al. (2007) designed a hyperspectral Compact Laboratory Spectro-Goniometer (CLabSpeG), which can effectively measure the BRF of a sample, using a halogen light source and an Analytical Spectral Devices (ASD) (Analytical Spectral Devices Inc., Boulder, CO) spectroradiometer. It has two half-circular arcs to support the zenith movement of the light source and the sensor. Furthermore, the light source and the sensor are mounted sideways of the arcs so as to minimize shadowing effects in the principal plane. The CLabSpeG can obtain a full hemispherical coverage with a resolution of 30° in azimuth and 15° in zenith directions, respectively.

To reduce the hot spot shadowing problem, a series of goniometer instruments have been developed in the remote sensing research laboratory at the University of Lethbridge. The current design of these systems is based on the use of a unique quarter circle arc that allows for a simplified, light-weight and faster positioning system compared with existing designs (University of Lethbridge Goniometer System 2.0 (ULGS-2.0)) (Coburn and Noble 2009). With this design, the hot spot shadow can be avoided if the starting measurement is at 5° away from the solar (light) principal plane. Due to the quarter circle arc, no shadow will be created once the arc is positioned in the forward-scattering direction, which is the advantage compared with FIGOS, SFG or CLabSpeG instruments. A further advance, ULGS version 2.5 (ULGS-2.5), can carry a heavy payload for image-based BRF sampling and can acquire angular data from 0° to 60° view zenith angle over the full 360° azimuth with an angular interval of 20° in both dimensions.

The objectives of this study were (1) to investigate the difference between BRF characteristics of rough and smooth surfaces using both image-based and non-image based data; and (2) to study the influence of spatial scene components on soil BRF.

MATERIALS AND METHODS

A soil sample from the experimental farm of the Lethbridge Research Centre (lat. 112°42′38.21″W, long. 49°40′57.64″N), Agriculture and Agri-Food Canada, was collected and naturally dried in the laboratory. The soil is Dark Brown Chernozemic clay loam (fine-loamy, mixed, Typic Haploborolls). The original soil sample with large clods was used as the rough surface to present the average soil surface roughness of a recently tilled field (Fig. 1a and c). After the initial measurements of the rough surface, the large clods were broken to generate a smooth surface (Fig. 1b), which would more closely represent the post-sowing soil condition, as the clods tend to decrease in size over time due to mechanical breakdown, wind and rain erosion (Fig. 1d).

Hyperspectral images of the soil samples were acquired at various angles using the ImSpector V10E imaging spectrometer (IS) mounted on the ULGS-2.5 and the spectral reflectances were computed with the help of a cross-calibration between the IS and the ASD FieldSpec®3 (350–2500 nm). The ImSpector V10E IS consists of a Hamamatsu C8484-05G camera, a V10E spectrograph, a 1.9/35 mm C-mount zoom lens, and a mirror scanner (Fig. 2). The Hamamatsu C8484-05G is a high spectral resolution digital camera. The V10E spectrograph has a slit size of 30 μm by 14.3 mm and can collect hyperspectral imagery in the wavelength range of 400–1000 nm with a spectral resolution of 2.8 nm. Together with the mirror scanner, the Hamamatsu C8484-05G collects the images in a push-broom manner and generates hyperspectral images with effective pixels of 1344 (spatial axis) by 1024 (spectral axis). In this study, the image was binned 4 by 4 to improve the signal/noise ratio, which resulted in a final image size of 336 spatial by 256 spectral pixels. The angular field of view of the IS is 14° (horizontal) by 11° (vertical). Under our observation strategy, the camera faced downward at a distance of 1780 mm above the target (Fig. 2). The image footprint is a rectangle, with a size 437 mm by 343 mm when viewing at nadir. When positioning the IS at 20°, 40° and 60° viewing zenith angle, the image footprints are trapeziums with a longer base at 455 mm, 478 mm and 705 mm, a shorter base at 424 mm, 406 mm, and 376 mm, and a height at 356 mm, 450 mm and 705 mm, respectively (Fig. 3). The pixel size at nadir is

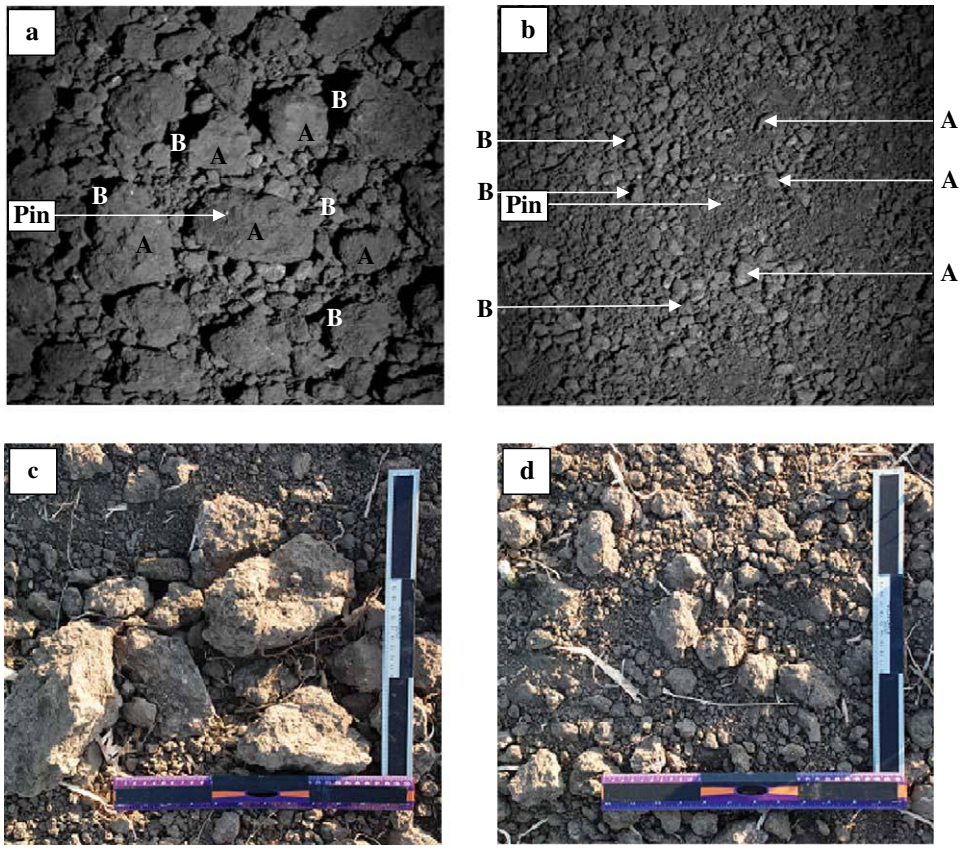

Fig. 1. Rough (a and c) and smooth (b and d) soil surfaces and their scene components. A represents the illuminated scene component, and B represents the shaded scene component. The point in the centre of the image is the push pin. Plates c and d represent the recently tilled rough and smooth soil surface, respectively.

1.3 mm by 1.3 mm. The biggest clod size in our experiment is about 120 mm by 50 mm.

The hyperspectral images were collected in a dark room. The soil samples were illuminated at 30°, 45° and 60° zenith angles by a 750 watt halogen light source, with a 15° spotlight lens to provide a degree of collimation of the incident illumination. The spotlights were mounted at 1.60 m, 2.77 m and 4.79 m above the floor on a stand, which was 2.77 m away the centre of the FOV of the IS, to create 30°, 45° and 60° illumination zenith angles and were allowed to thermally stabilize by remaining on for an hour before measurements were taken.

The angle between the light principal plane (LPP) and the boom of the goniometer was 120° for 30° and 45° illumination zenith angles and was 110° for 60° illumination zenith angle. Room temperature was around 21.5°C through the BRF data sampling. A small green pin was placed at the exact centre of the nadir field of view (FOV) of the IS to centre all the images (Fig. 1a and b). When operating the ULGS-2.5, both the quarter-arc and the IS were moved manually to acquire data from 0° to 60° view zenith angles over the full 360° azimuth range at an angular interval of 20° in both dimensions. Only the analysis of data acquired under 30° illumination angle is presented in this paper.

The image acquisition sequence is shown in Fig. 4 (a). The image acquisition process was controlled by the CSIspec-IS-lite software (Channel Systems Inc., Manitoba, Canada). The exposure time was set at 12 ms throughout the BRF data sampling. The size of the images at nadir, 20°, 40°, and 60° zenith angles were 336 by 324 pixels, 336 by 324 pixels, 336 by 376 pixels and 336 by 430 pixels because scan lengths were set at 600, 600, 700 and 800 mm for the above four viewing zenith angles, respectively. All the images included 256 spectral bands within the 400–1000 nm range. Fifty-five images were taken in about 30 min. The relative light intensity was recorded 5 min, 4 min, 3 min, 2 min, 1 min, 40 s, and 20 s before and 20 s, 40 s, 1 min, 2 min, 3 min, 4 min, and 5 min after the images acquisition using an ASD measured over a Spectralon panel. During the 40 min, the light intensity increased about 1% from the beginning to the end of the measurement.

Each hyperspectral image acquired was sent to a laptop computer through an IEEE 1394 cable. All images were processed and analyzed using ENVI 4.5 (Environment for Visualizing Images, Research Systems

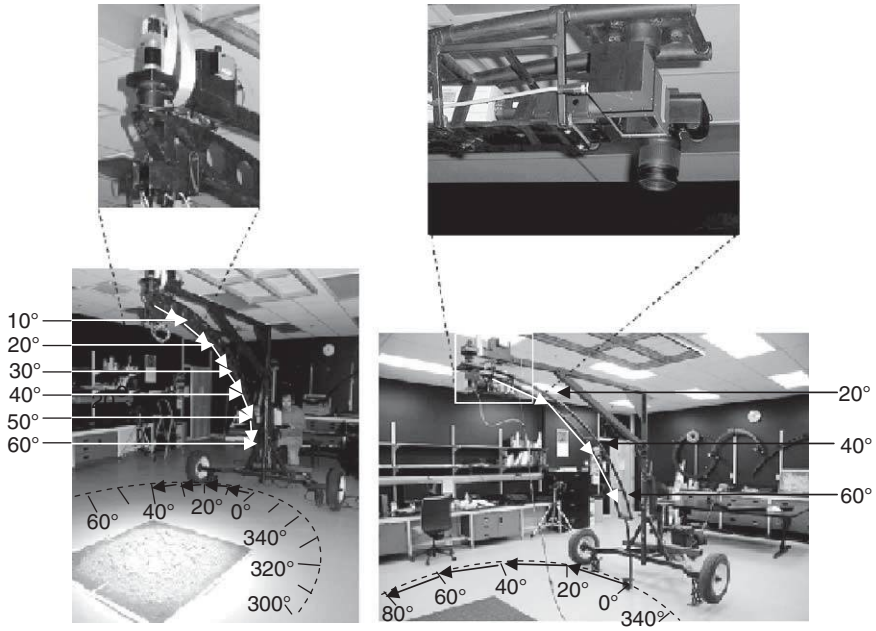

Fig. 2. Laboratory use of the ULGS-2.0 (left) with Ocean Optics and the ULGS-2.5 (right) with an ImSpector V10E imaging spectrometer mounted on the arc, respectively. The angles on both left and right sides of the pictures are viewing zenith angles, which represent the positions of the Ocean Optics and the imaging spectrometer on the quarter circle arcs of the ULGS-2.0 and the ULGS-2.5, respectively. The broken arc lines represent the tracks of the quarter circle arcs of both ULGS-2.0 and ULGS-2.5 on the floor, and the angles along the arc line represent the viewing azimuth angles. The downward and counter-clockwise arrows along the ULGS arcs and the broken arc lines represent the moving directions of the Ocean Optics (or the imaging spectrometer) on the ULGS arc and the ULGS arcs in the azimuth direction, respectively.

Inc., Boulder, CO). A circular region of interest (ROI) with a diameter of 140 pixels around the pin, where the light intensity varied 1% from the centre to the edge of the ROI, was used for BRF development. Illuminated and shaded scene components were extracted by ISODATA unsupervised classification as the scene components (Fig. 5). The mean reflectance of the whole ROI was used for whole ROI BRF plots development, and those of the illuminated scene component and the shaded scene component were used to develop BRF plots of illuminated and shaded scene components, respectively.

To correct the images for the dark current of the camera, a dark image was obtained in the same dark room as for sample image acquisition by covering the IS with a thick black cloth. It was not feasible for the IS to make measurements over a Spectralon panel to acquire a white reference, as its FOV was larger than the area of the Spectralon panel. In this research, the white reference data measured by the ASD under the same view/illumination geometry condition as for the soil sample were employed to calculate reflectance of the imaged soil. A cross-calibration between the IS and the ASD was performed on the roof of the building on a sunny day. Both the IS and the ASD were set side by side at a height of 800 mm above a coloured felt panel (Fig. 6). The tripods supporting the IS and the ASD were put on the north side of the coloured felt panel to avoid the shadow casting on the board. Through the CSIspec-IS-lite software, the scan length of the IS was set at 200 mm. It took about 5 s to record the 200 mm long image. The ASD readings acquisition interval was set at one reading per operation. When performing the cross-calibration, the 200 mm long image was acquired first. Then operated the ASD 2 s after the image acquisition to ensure that both the IS and the ASD sensed the same area on the coloured felt panel. Once the data of one colour were finished, another colour was moved under the two systems and its position was adjusted to ensure that the FOV of the two sensor systems were inside the same colour region. Seven colour targets were measured. The procedures were repeated five times for each colour target.

The reflectance of the imaged soil surface was calculated using the following equation.

$$\rho_{soil(\lambda)} = \left[\frac{(Q_{soil} - Q_d)_{SD\lambda}}{(DC_p - DC_d)_{ASD\lambda'}}\right]\left(\frac{DC_{ASD}}{Q_{ct}}\right)_{\lambda\lambda'}(F_P)_{\lambda''} \quad (3)$$

where ρ_{soil} is the spectral reflectance of the soil sample, Q_{soil} is the digital counts of the soil, Q_d is the digital counts of the dark image measured with IS or Ocean Optics (OO) USB-4000, SD following ($Q_{soil} - Q_d$) is spectrometer device, which refers to IS here and OO below for spectral reflectance of the non-imaged soil sample, DC_p is the digital counts of the Spectralon panel

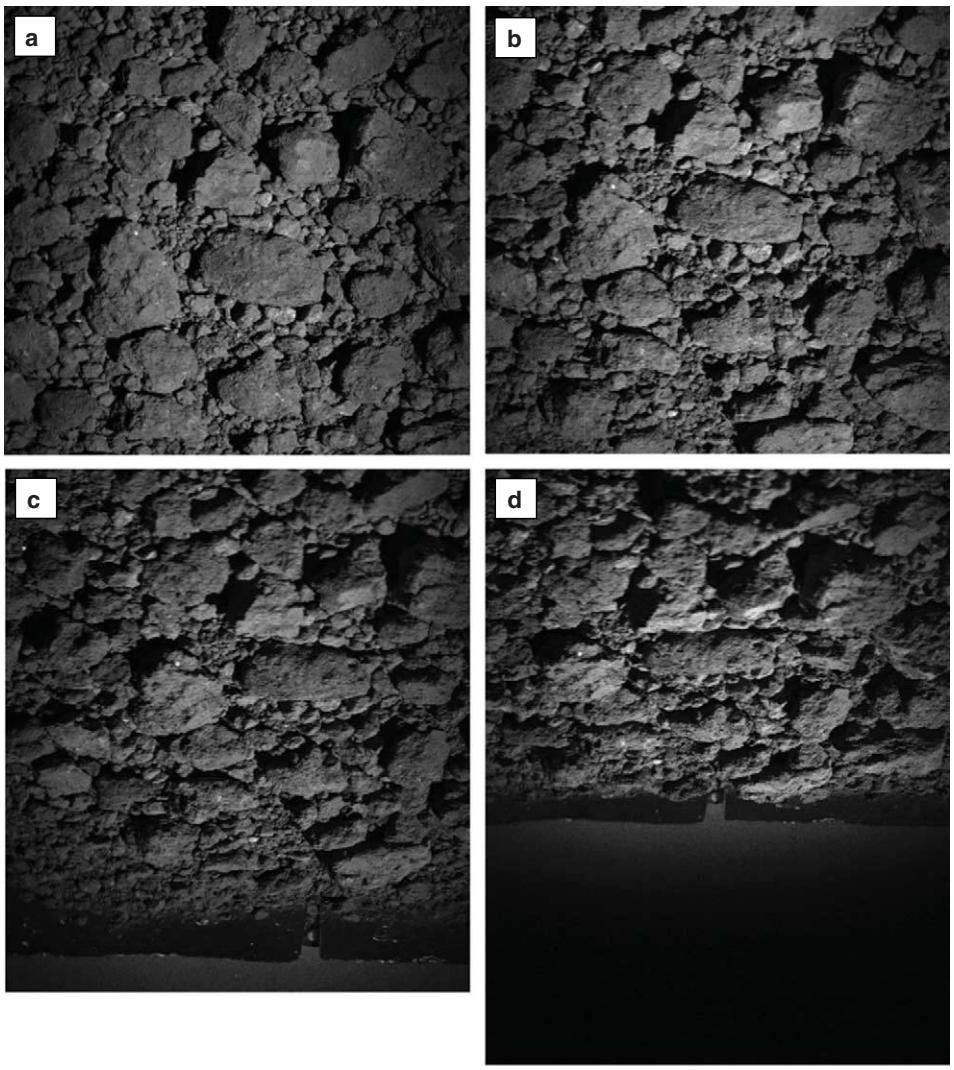

Fig. 3. The full image of the rough soil surface acquired at nadir (a), 20° (b), 40° (c) and 60° (d) viewing zenith angles, respectively. The part in the bottom of c and d is the floor of the laboratory.

measured by ASD under the same illumination conditions as for the soil sample, DC_d is the digital counts measured with the ASD fibre optic cable was covered with the thick black cloth in the dark room, DC_{ASD} is the digital counts of the colour target measured by ASD in the cross-calibration campaign, Q_{ct} is the digital counts of the colour target measured by IS or OO in the cross-calibration campaign, F_p is the spectral reflectance factor of the Spectralon panel, and λ, λ' and λ'' are wavelengths of the IS (or OO), ASD and the Spectralon panel reflectance factor, respectively. The λ, λ' and λ'' were interpolated to the same wavelength grid to calculate the ρ_{soil}.

An OO USB-4000, equipped with an 8° FOV barrel, was mounted on the ULGS-2.0 to collect the soil radiance (i.e., non-image based data) over the range of 350–1000 nm. The USB-4000 has variable integration times and can sample 10 radiance readings in ≤ 0.5 s. At this rate, the total time required to acquire a full BRF dataset, as defined above, is 12 min. The quarter-arc of the ULGS-2.0 was mounted on a computer-controlled stepper motor using a gear-reduction transmission. This design ensures the positioning of the arc within very close tolerances. The sensor sled, which houses the upwelling sensor, was driven by a computer-controlled stepper motor that drives the sled using a rack mounted on the arc. The instrument also incorporated an additional downwelling sensor equipped with a cosine corrector head (which was not used for the indoor measurement). To correct the radiance for the dark current of the OO spectrometer, a dark calibration was performed by capping the sensor head and a white calibration was performed by looking at a Spectralon panel placed at the same level as the soil surface and

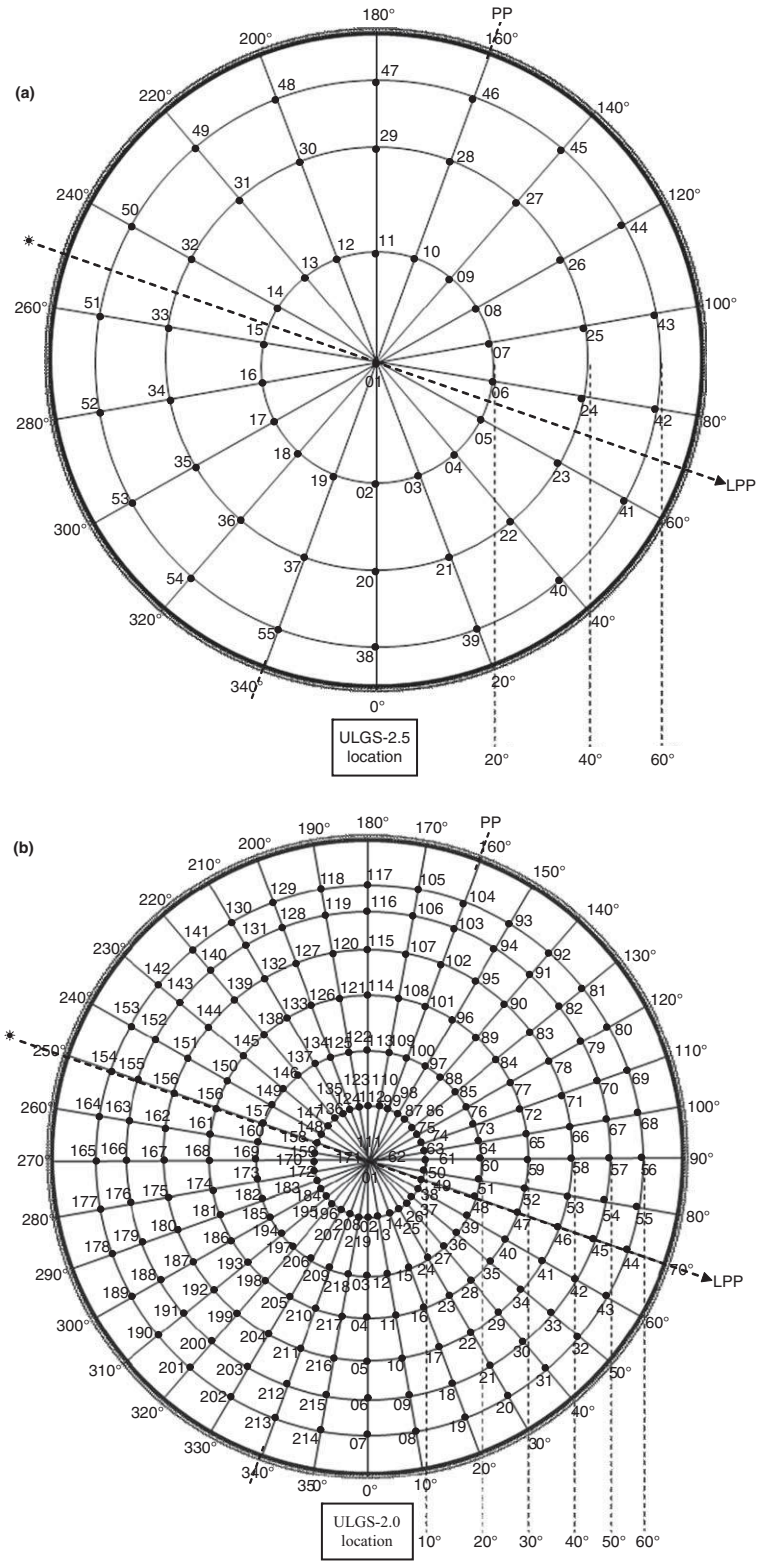

Fig. 4. (a) Sampling sequence of the imaging spectrometer mounted on the ULGS-2.5. The dashed line arrow represents the illumination direction. LPP is light principal plane and PP is perpendicular plane. (b) Sampling sequence of the Ocean Optics USB-4000 mounted on the ULGS-2.0. The dashed line arrow represents the illumination direction. LPP is light principal plane and PP is perpendicular plane.

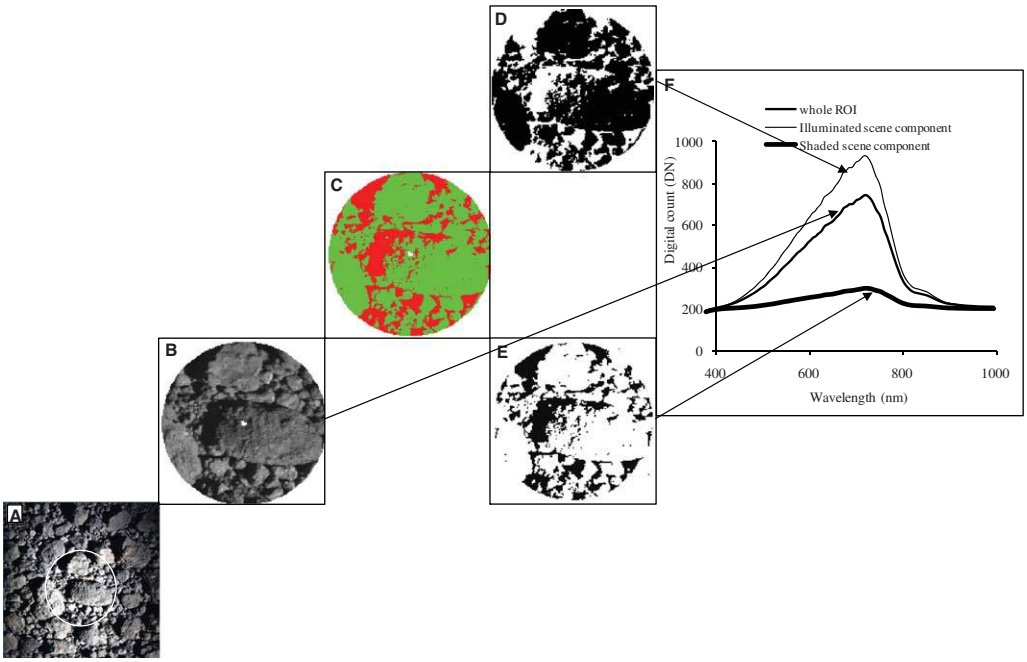

Fig. 5. Scene components extraction steps of the image-based BRF. A, B, C, D, E, and F are the acquired image, the subset region of interest (ROI), classified ROI, illuminated scene component, shaded scene component, and spectral profiles of the whole ROI, illuminated scene component and shaded scene component, respectively. The same procedures were applied to the smooth surface.

centred in the focus of the light spot. The ULGS-2.0 acquires angular data from 0° to 60° zenith angles over the 360° azimuth range with an angular resolution of 10° in both dimensions. Besides the starting nadir measurment, the sled got back to nadir again at 90°, 180°, and 270° azimuth to acquire additional nadir data. A total of 220 unique points were acquired over a full measurement sequence (Fig. 4b). The reflectances of the investigated bands were extracted by using G3D, software developed by the Department of Geography of the University of Lethbridge, from the ULGS-2.0 processed dataset for BRF construction.

A cross-calibration between the OO and ASD was performed under natural illumination conditions. The same procedures used in the cross-calibration between IS and ASD were used. Both the IS and the OO were calibrated to the same ASD (Eq. 3), which ensured that comparison between the two sensing systems was possible.

Before the BRF sampling by ImSpector V10E IS mounted on the ULGS-2.5 and OO USB-4000 mounted on the ULGS-2.0, the DC of both the rough and smooth soil surfaces were recorded by the ASD and were computed to soil spectral reflectance thereafter. ASD recorded the DC from 350 nm to 2500 nm. Since the maximum wavelength of both the ImSpector V10E IS and the OO USB-4000 is 1000 nm, the wavelength range of the soil spectral reflectances of both rough and smooth surfaces measured by the ASD was limited to 400–1000 nm (Fig. 7).

Surface roughness measurements were carried out with a ShapeGrabber 3D (3 dimensional) laser scanner for both the rough and smooth surfaces after the BRF sampling was completed. The scanner was mounted on a tripod that was moved around the soil sample to scan an approximately 0.25 m^2 plot from four different azimuthal directions. The 3D measurements for both soil surface roughness categories were conducted under dark conditions. The 3D scanner source data were transformed to a set of points with x, y and z coordinates. The z coordinates (relative to the data minima) were used to calculate soil surface roughness using the coefficient of variation (CV) of the values (Garća Moreno et al. 2008, 2010).

$$SD = \sqrt{\frac{1}{N-1}\sum_{i=1}^{N}[z(n_i) - \bar{z}]^2} \quad (4)$$

$$CV = \frac{SD}{\bar{z}} * 100\% \quad (5)$$

where SD is standard deviation, n_i is the location of the ith measurement and $z(n_i)$ is the elevation (a soil topographical parameter), $\bar{z}$ is the average value of set $z(n_i)$(μm) and N is the number of data points (100 000 for the rough surface and 70 000 for the smooth surface in this study). The surface roughness index (SRI, i.e., CV of the z values) of the rough surface was 51% and that of the smooth one was 5%. The distribution of the z values is shown in Fig. 8.

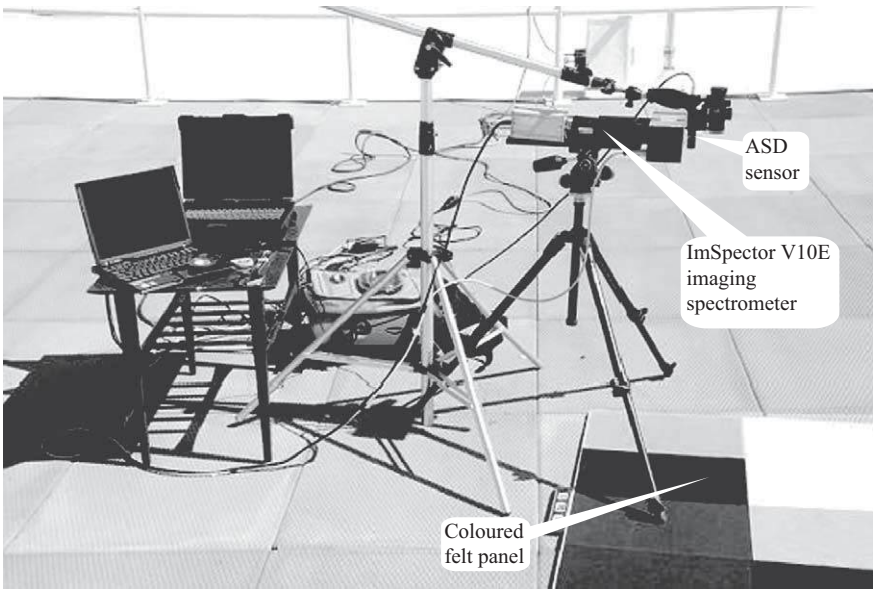

Fig. 6. Cross-calibration between the ImSpector V10E imaging spectrometer and the ASD. The bottom of the mirror scanner of the ImSpector V10E imaging spectrometer and the end of the ASD sensor were set at the same level above a coloured felt panel.

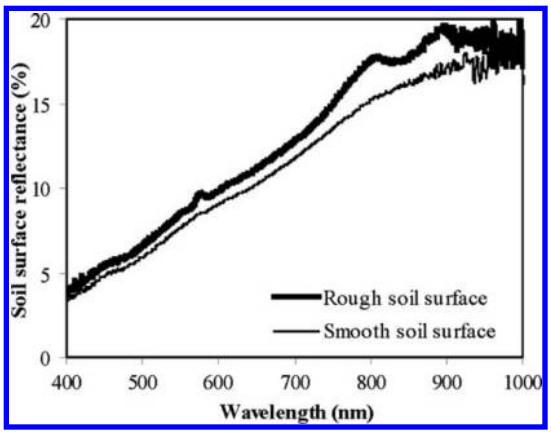

Fig. 7. Spectra of soil measured with an ASD viewing at nadir.

Two-dimensional (2D) representations of both the non-image based and the image-based BRF were generated by ArcGIS 9.3 [Environmental Systems Research Institute (ESRI), Inc., Redlands, CA]. Each viewing point was projected onto a flat surface at the level of the soil surface. The projection was done using Eqs. 6 and 7.

$$X_i = l \sin(\theta_v)\cos(\phi_v) \tag{6}$$

$$Y_i = l \sin(\theta_v)\sin(\phi_v) \tag{7}$$

where l is the goniometer arc radius, i is an index for images in a given data acquisition run, and θ_v and ϕ_v are viewing zenith and viewing azimuth angles, respectively. The data affected by the arc shadow were removed and replaced by interpolated values using a quadratic polynomial interpolation method. The angular sampling interval of the ULGS-2.5 and the ULGS-2.0 are 20° and 10°, respectively, in both zenith and azimuth dimensions (Fig. 4a and b). To make the BRF plot of the non-image based data comparable with those of the image-based data, the angular sampling interval of the non-image based data was reduced to 20° in both zenith and azimuth dimensions when developing the BRF plot (Fig. 9).

The BRF plots for image and non-image based data, rough and smooth surface, and image-based whole ROI and scene components were compared using the similarity index, which was calculated using the Czekanowski's Quantitative Index (CQI) (Bloom 1981).

$$CQI_{ik} = \frac{2\sum_{i=1}^{S} \min(x_{ai}, x_{bi})}{\sum_{i=1}^{S} (x_{ai} + x_{bi})} \tag{8}$$

Where S is the number of observations in samples a and b; x_{ai} is the ith observation in sample a, x_{bi} is the ith observation in sample b. Under our research condition, the CQI ranged from 0.43 to 0.98 (Table 1).

RESULTS AND DISCUSSION

Soil Surface BRF of Rough and Smooth Soil Surfaces under 30° Illumination Zenith Angle

The BRF plots were symmetrical along the LPP of both the non-image based and image-based data, with an exception of non-image based data of the smooth surface at 860 nm, which was quite asymmetrical.

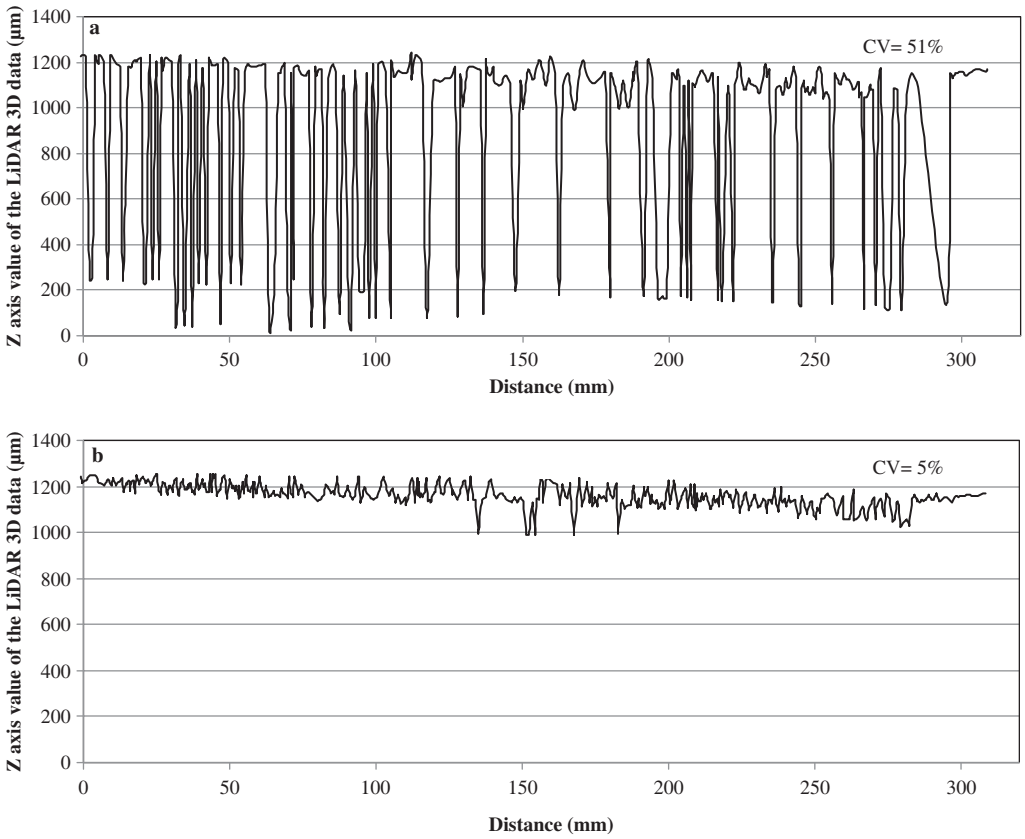

Fig. 8. The distribution of the Z axis value of the ShapeGrabber 3D data for both rough (a) and smooth soil surface (b).

As shown in Figs. 9, 10 and 11, the BRF plot of the rough surface had similar patterns (similarity index ranged from 0.94 to 0.98, Table 1), with respect to the viewing geometries, as those of the smooth surface for the non-image based data and the whole ROI of the image-based data. This suggests that under laboratory conditions using a spotlight as the light source, the rough soil surface exhibited similar BRF characteristics as the smooth surface. The similarity between rough and smooth soil surfaces under natural environment need to be determined in the future.

Compared with the smooth surface, the rough surface exhibited higher surface reflectance under most of the viewing angles (Fig. 12, Fig. 13 and Fig. 14).

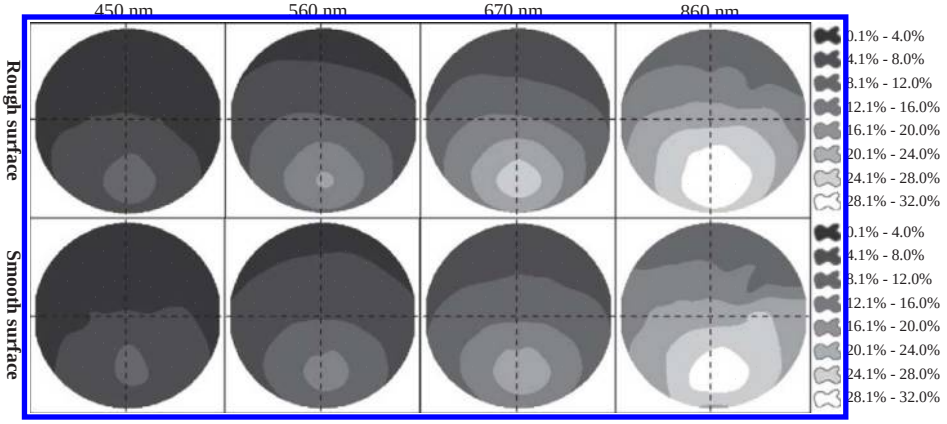

Fig. 9. The non-image based BRF plots of the rough and smooth soil surface under 30° illumination zenith angle. Both the zenith and azimuth sampling intervals were reduced to 20° to match the sampling intervals of the imaging system. The vertical and horizontal dashed lines represent light principal plane (LPP) and perpendicular plane (PP), respectively.

Table 1. The similarity indices of BRF plots between image and non-image data, between rough and smooth soil surface, between imaged whole ROI and illuminated scene component, and between imaged whole ROI and shaded scene component

	Wavebands			
	450 nm	560 nm	670 nm	860 nm
Image rough vs. non-image rough	0.81	0.87	0.86	0.77
Image smooth vs. non-image smooth	0.81	0.86	0.85	0.77
Image rough vs. image smooth	0.97	0.95	0.94	0.98
Non-image rough vs. non-image smooth	0.97	0.96	0.96	0.98
Image rough whole ROI vs. illuminated scene component	0.84	0.85	0.85	0.85
Image rough whole ROI vs. shaded scene component	0.55	0.58	0.59	0.61
Image rough illuminated scene component vs. shaded scene component	0.43	0.47	0.47	0.49
Image smooth whole ROI vs. illuminated scene component	0.94	0.94	0.94	0.95
Image smooth whole ROI vs. shaded scene component	0.77	0.75	0.75	0.81
Image smooth illuminated scene component vs. shaded scene component	0.72	0.69	0.69	0.76

For non-image data, the average spectral reflectance of all the measured points of the rough surface were 2.7 (absolute value, in percentage, the same below) (37.4% relatively) at 450 nm, 4.0 (39.8% relatively) at 560 nm, 4.0 (39.5% relatively) at 670 nm and 2.5 (12.3% relatively) at 860 nm higher than those of the smooth surface. The figure for the image-based data were −0.04 (−1.2% relatively), 1.0 (10.5% relatively), 1.2 (11.0% relatively) and 0.1 (0.2% relatively) at 450, 560, 670 and 860 nm, respectively. The higher spectral reflectance in the rough surface could also be seen in Fig. 7, where the spectral reflectances of both rough and smooth surfaces were measured using the ASD. The BRF plots of the image-based data were not identical to those of the non-image based because the FOV is different to those of the image-based data. Even for the non-image based data, the FOVs are different at different viewing zenith angles. The authors tried to reduce the ROI to half of the biggest clod and found that the BRF of the ROI of half the biggest clod was highly similar to those of the ROI reported in this study for whole ROI and scene components. This suggested that the FOV of the IS had no affect on the BRF of the soil surface under controlled laboratory conditions. Jacquemoud et al. (1992) proposed that the level of moisture content might affect the reflectance behaviour of smooth soil, and the drying could cause a decrease of the specular effect. Croft et al. (2009) stated that soil roughness effects had the strongest effect on albedo when soils were dry. Therefore, the drying decreased the spectral reflectance of the smooth soil surface.

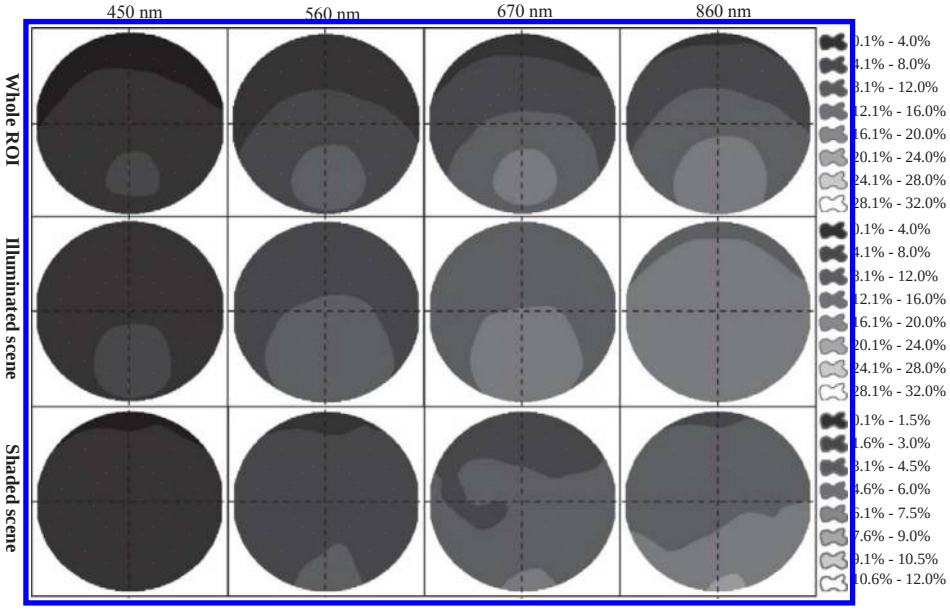

Fig. 10. The image-based BRF plots of the rough soil surface developed with the whole ROI, illuminated scene component and scene component, respectively. Both the zenith and azimuth sampling intervals are 20°. The illumination zenith angle is 30°. The vertical and horizontal dashed lines represent light principal plane (LPP) and perpendicular plane (PP), respectively.

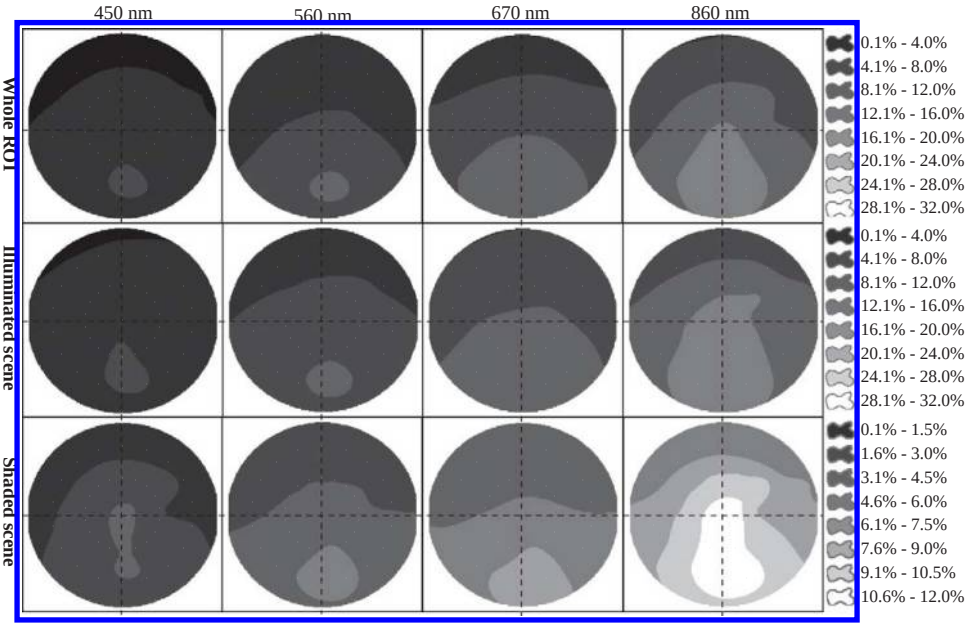

Fig. 11. The image-based BRF plot of the smooth soil surface developed with the whole ROI, illuminated scene component and shaded scene component, respectively. Both the zenith and azimuth sampling intervals are 20°. The illumination zenith angle is 30°. The vertical and horizontal dashed lines represent light principal plane (LPP) and perpendicular plane (PP), respectively.

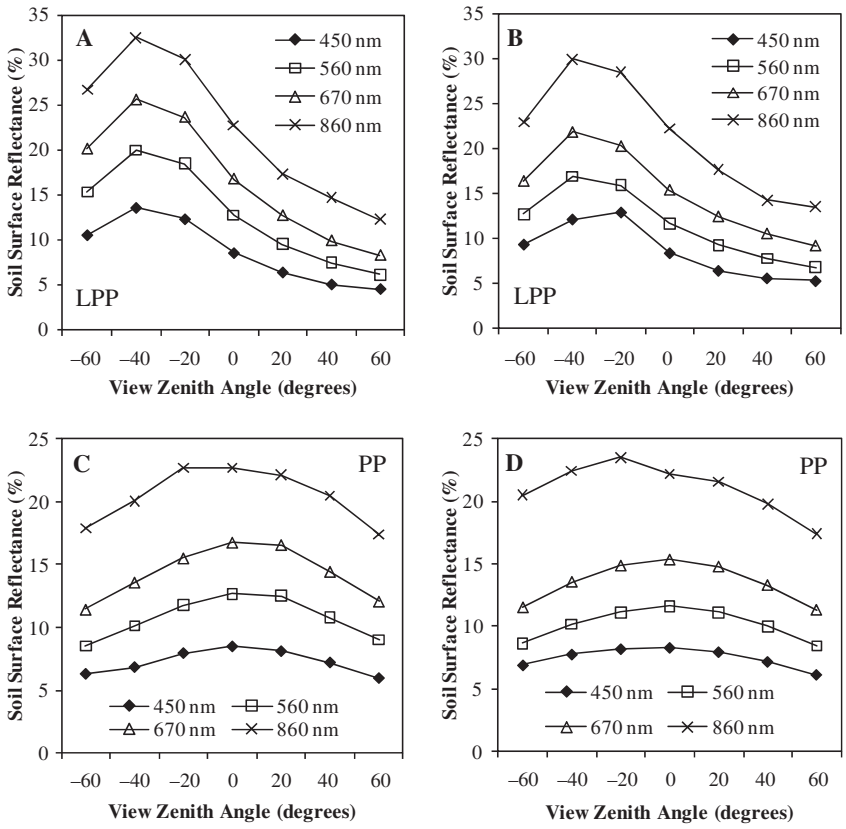

Fig. 12. Soil spectral reflectance of the non-image based data in the light principal plane (LPP) and the perpendicular plane (PP) of both the rough (A and C) and the smooth (B and D) soil surfaces under 30° illumination zenith angle.

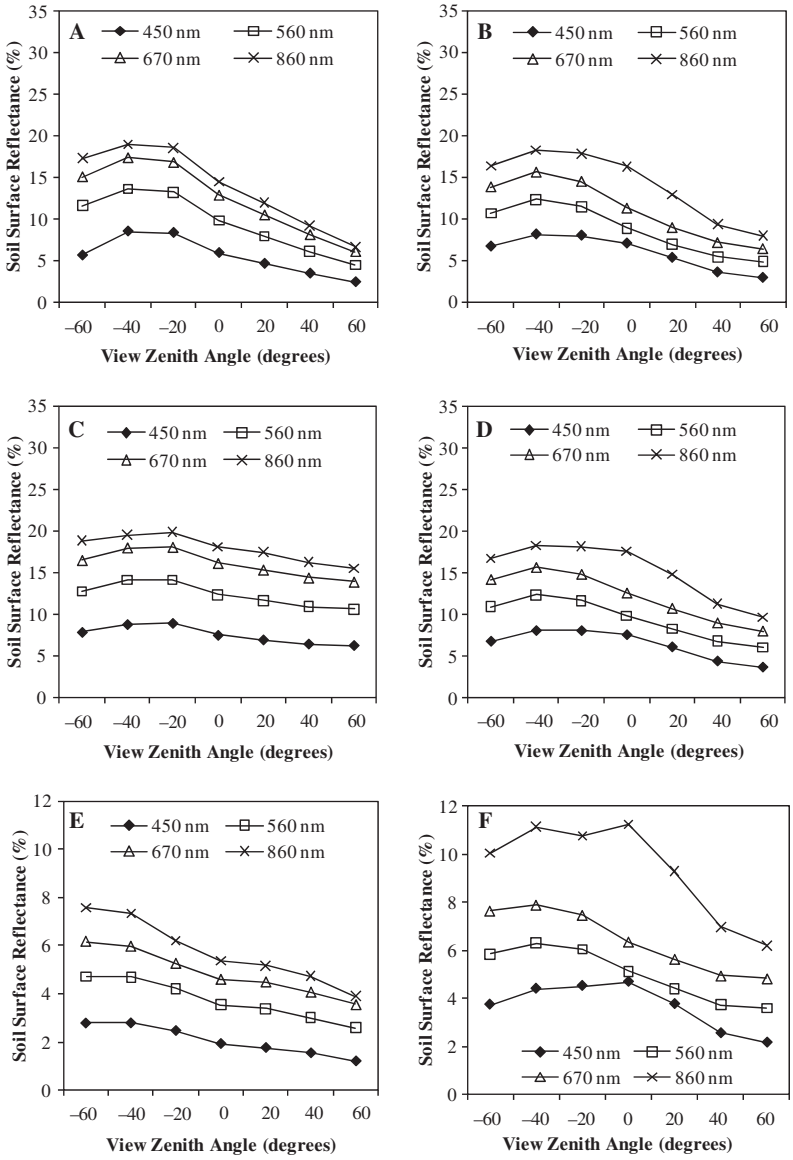

Fig. 13. Soil spectral reflectance of whole ROI (A and B), illuminated scene component (C and D) and shaded scene component (E and F) in the light principal plane (LPP) of both the rough (A, C and E) and the smooth (B, D and F) soil surfaces under 30° illumination zenith angle.

The hot spot occurred at −40° viewing zenith angle for both rough and smooth surfaces of the non-image based data and the whole ROI of the image-based data, with an exception of the non-image based data of the smooth surface at 450 nm which exhibited a hot spot at −20° viewing zenith angle (Figs. 12 and 13). As the illumination zenith angle was 30°, the hot spot would have occurred at −30° viewing zenith angle, an angle that was not measured by the IS in this study. For the non-image based data, the hot spot was observed at −30° for the non-image based before its angular sampling interval was reduced to 20° to match the imaging system (data not shown). In our observations with a maximum viewing zenith angle of 60°, the lowest reflectance in the forward scattering direction occurred at 60° viewing zenith angle for both soil roughness categories. Our research was in agreement with Cierniewski and Courault (1993) who reported that bare soil usually displays a minimum reflectance in the extreme forward-scattering direction near the horizon. Cierniewski et al. (2004) reported that bare soil typically shows maximum reflectance in the backscattering direction, where the particles hide their own shadow. When the viewing position was located at −40° zenith angle in the LPP, the dual activities of both illumination and viewing geometries enhanced the hiding effects and

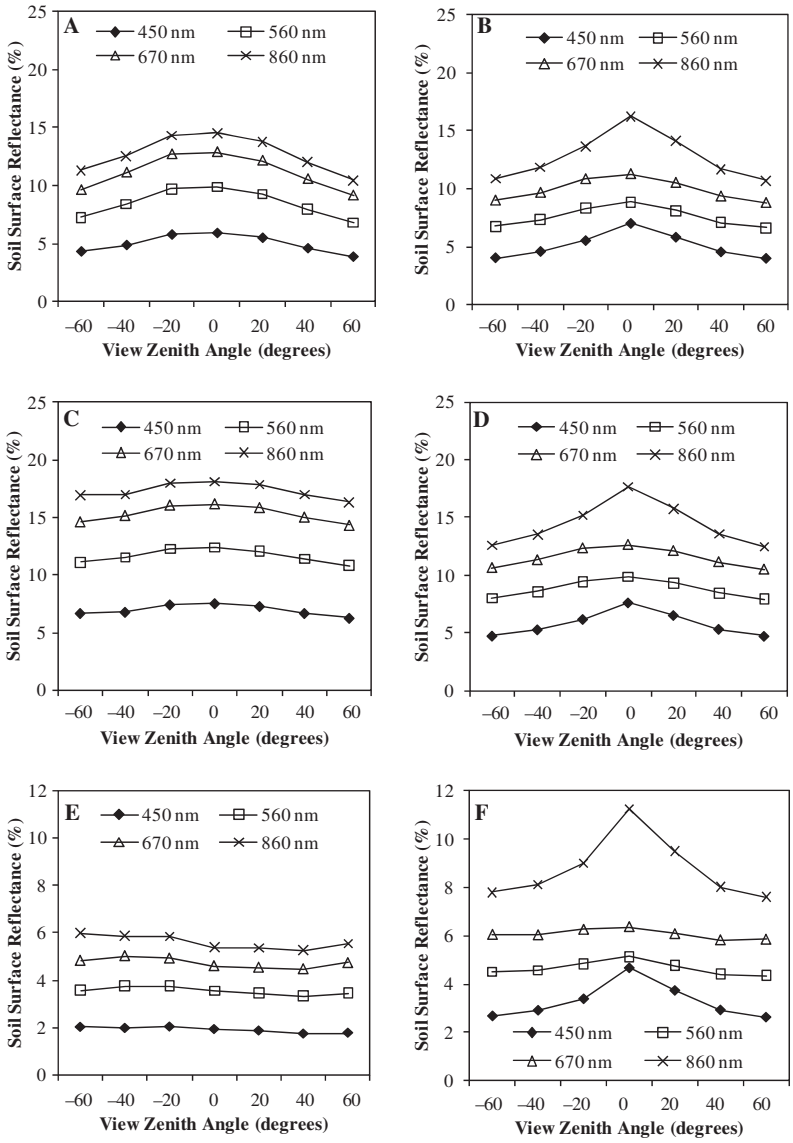

Fig. 14. Soil spectral reflectance of the whole ROI (A and B), illuminated scene component (C and D) and shaded scene component (E and F) in the perpendicular plane (PP) of both the rough (A, C and E) and the smooth (B, D and F) soil surfaces under 30° illumination zenith angle.

generated the highest soil reflectance at this point. Under our research condition with ImSpector V10E IS, the soil reflectance increased from 2.4% (at 450 nm) in the forward-scattering direction to 19.0% (at 860 nm) in the backscattering direction for the rough surface, and from 2.9% (at 450 nm) to 18.2% (at 860 nm) for the smooth surface. The variation of the reflectance in the rough surface is 8.5% higher than that in the smooth surface, suggesting that the rough soil exhibited greater BRF changes with view angle than did the smooth surface, which confirmed the statement of Jackson et al. (1990). Our observation confirmed that there was a wavelength dependent on the strength of the reflectance anisotropy.

A symmetrical BRF curve (i.e., a bell-shaped curve characterized with the spectral reflectance decrease with viewing point changes from nadir to higher zenith angle in same trend in both 90° and 270° azimuth direction) is expected in the perpendicular plane (PP) since the illumination condition is identical on both sides of the LPP. The case was observed for both soil surface roughness categories (Figs. 12 and 14). However, the reflectance was not equal at each symmetry point because the soil clods in the FOV of the IS were not regularly arranged. But the bell shape was more apparent for the smooth soil surface than for the rough soil surface, indicating that the spectral reflectance of the smooth soil surface varied more than the rough with

respect viewing zenith angle in the PP. The bell shape peaks of the shaded scene component in the rough surface were smooth. The possible reason is that the shadowing effect is more pronounced for the rough surface and approximate shaded proportions were observed at nadir (28.2%) and its two neighbour points (32.4% and 30.4%) in the PP.

Soil Surface BRF of Different Scene Components

The advantage of the image-based approach is that it allows the characterization of the impact of scene components on surface BRF, which is not possible with non-image based BRF investigations. In this study, the illuminated and shaded scene components of both rough and smooth surfaces were extracted to analyze the BRF characteristics of different scene components. The contribution of each scene component to the entire BRF was also presented in this study. Many studies have worked on the shadowing effect on soil spectral reflectance characteristics and demonstrated that shadow is an important factor influencing the shape of the surface radiation pattern (Cierniewski 1987; Huete and Warrick 1990; Irons et al. 1992). To our knowledge, no earlier published work has specifically studied the influence of the scene components on the soil BRF.

Our research demonstrates that the BRF pattern of the whole ROI of the image-based data was similar to that of the illuminated scene component, especially for the smooth surface (Table 1, Fig. 10 and Fig. 11). The BRF pattern of the shaded scene component was different from that of the whole ROI and the illuminated scene component for the rough surface, not only showing in the pattern, but also showing in the reflectances. However, the BRF pattern of the shaded scene component of the smooth surface was similar to those of the whole ROI and the illuminated scene component (Table 1).

The hot spot occurred at -40° viewing zenith angle for the whole ROI, illuminated and shaded scene components of the smooth surface. However, the hot spot occurred at -40, -20 and -60° viewing zenith angles, for the whole ROI, illuminated and shaded scene components of the rough surface, respectively. The hot spot variation in the rough surface might attribute to its pronounced shadowing effect. In the LPP, the percentage of the illuminated scene component in the whole ROI was 28.4, 38.9, 55.1, 71.8, 88.5, 91.9, and 82.3%, respectively, for the rough surface when viewing angle changed from 60 to -60° under 30° illumination angle. The figures for the smooth surface were 50.2, 54.3, 65.1, 78.7, 92.2, 95.5, and 91.2%, respectively.

The above results indicate that more shadows were seen by the IS when sensing from a forward scattering direction than sensing from nadir and much more than sensing from a backscattering direction. In other words, the fewer shadow the IS is seeing, the higher spectral reflectance of the soil appears. The soil surface reflectances of the illuminated scene component were generally higher than those of the whole ROI, especially those at the forward scattering angles because the shadowing effect was more apparent in the forward scattering direction than in the backscattering direction. In addition, the shadow effect was stronger in the rough soil surface, as reported by Richter et al. (2005). In the LPP, the illuminated scene component followed the pattern of the whole ROI, but the shaded did not. The contribution of the shadow in the forward-scattering direction is more apparent for the rough than for the smooth surface. The greater difference among the four investigated wavelengths was observed at the viewing points in the backscattering direction compared with those in the forward-scattering direction for the whole ROI, illuminated scene component and shaded scene components in both soil categories (Fig. 13), suggesting that the backscattering enhancement of the spectral reflectance was wavelength-dependent (Peltoniemi et al. 2005).

In the PP, bell-shaped BRF curves were observed for whole ROI and illuminated scene component of the two surface categories and for the shaded scene component of the smooth surface (Fig. 14). The bell shape was more apparent for the whole ROI than for the illuminated scene component of the rough surface. No bell-shape pattern was shown for the shaded scene component of the rough surface at all the four investigated wavelengths. In the PP, the smallest difference among the four investigated wavelengths occurred at the 60° viewing zenith angle and the largest difference showed at the peak area of the BRF curve for the smooth surface. However, the BRF showed similar patterns in the PP among the four investigated wavelengths for the rough surface.

CONCLUSIONS

An improved understanding of the soil surface bidirectional reflectance patterns is essential to improve the interpretation accuracy of satellite or airborne remotely sensed data. The research reported in this paper used both an image-based and a non-image based approach to sample BRF to assess the roles of soil surface roughness and spatial scene components on the BRF signal. The results generated from both the image-based and the non-image-based data confirmed the expectation that the BRF of the rough soil surface was more sensitive to viewing geometry than was the smooth surface. The shadowing effect was stronger in the rough soil surface than in the smooth surface and stronger in the forward scattering direction than in the backscattering direction. The results showed that the pattern of the BRF generated with the non-image based data was similar to that generated with the whole ROI of the image-based data, and the BRF pattern of the whole ROI was similar to that of the illuminated scene component of the image-based data. The hot spot varied in angle location among the whole ROI, illuminated and shaded scene component for the rough surface, but it

was quite stable for the smooth surface. Since our sample was dry and illuminated by a spotlight, the rough soil surface exhibited higher spectral reflectance than the smooth surface under most of the viewing angles. The BRF of the smooth soil surface was dominated by the illuminated scene component, whereas the shaded scene component was a larger component of the BRF of the rough soil surface. Unlike the view zenith angle dependence of the illuminated and shaded scene component, the view zenith angle dependence of the whole ROI showed a pronounced bell-shaped curve in the PP. The image-based approach allows the characterization of the impact of spatial scene components on soil BRF, which is not possible with non-image based BRF investigations. Our results indicate that the sub-pixel architecture is a significant contributor to the observed BRF. If the spatial resolution of the IS is enhanced, the percentage of the mixed pixels of sunlit/shadow will be decreased (i.e., the number of both pure sunlit and pure shadow pixels will be increased) and more details of the scene components could be discussed. Therefore, the character of the scene component could be described more accurately.

Future research should concern the effect of soil moisture on soil BRF and the variation of the BRF of soil surfaces in the shortwave infrared region. Special attention needs to be given to how the soil moisture and surface roughness affect the vegetation canopy spectral reflectance.

ACKNOWLEDGEMENTS

This research was supported by Alberta Ingenuity funding. The authors also wish to thank the Natural Sciences and Engineering Research Council of Canada for the grant to purchase the ShapeGrabber 3D laser scanner.

Barnsley, M. J., Hobson, P. D., Hyman, A. H., Lucht, W., Muller, J.-P. and Strahler, A. H. 2000. Characterizing the spatial variability of broadband albedo in a semidesert environment for MODIS validation. Remote Sens. Environ. **74**: 58–68.

Barnsley, M. J., Lewis, P., Sutherland, M. and Muller, J.-P. 1997. Estimating land surface albedo in the HAPEX-Sahel southern super-site: inversion of two BRDF models against multiple angle ASAS images. J. Hydrol. **188–189**: 749–778.

Barnsley, M. J., Morris, K. P., Strahler, A. H. and Muller, J.-P. 1994. Sampling the surface bidirectional reflectance distribution function (BRDF): Evaluation of current and future satellite sensors. Remote Sens. Rev. **8**: 893–916.

Ben-Dor, E., Chabrillat, S., Demattê, J. A. M., Taylor, G. R., Hill, J., Whiting, M. L. and Sommer, S. 2009. Using imaging spectroscopy to study soil properties. Remote Sens. Environ. **113**: 38–55.

Ben-Dor, E., Patkin, K., Banin, A. and Karnieli, A. 2002. Mapping of several soil properties using DAIS-7915 hyperspectral scanner data-a case study over clayey soils in Israel. Int. J. Remote Sens. **23**: 1043–1062.

Biliouris, D., Verstraeten, W. W., Dutré, P., van Aardt, J. A. N., Muys, B. and Coppin, P. 2007. A compact laboratory spectro-goniometer (CLabSpeG) to assess the BRDF of materials. Presentation, calibration and implementation on *Fagus sylvatica* L. leaves. Sensors **7**: 1846–1870.

Bloom, S. A. 1981. Similarity indices in community studies: potential pitfalls. Mar. Ecol. Prog. Ser. **5**: 125–138.

Chang, C. W. and Laird, D. A. 2002. Near-infrared reflectance spectroscopic analysis of soil C and N. Soil Sci. **167**: 110–116.

Cierniewski, J. 1987. A model for soil surface roughness influence on the spectral response of bare soils in the visible and near-infrared range. Remote Sens. Environ. **23**: 97–115.

Cierniewski, C. and Courault, D. 1993. Bidirectional reflectance of bare soil surfaces in the visible and near-infrared range. Remote Sens. Rev. **7**: 321–339.

Cierniewski, J. and Kuśnierek, K. 2010. Influence of several size properties on soil surface reflectance. Quaestiones Geographicae **29**: 13–25.

Cierniewski, J., Gdala., T. and Karnieli, A. 2004. A hemispherical–directional reflectance model as a tool for understanding image distinctions between cultivated and uncultivated bare surfaces. Remote Sens. Environ. **90**: 505–523.

Cierniewski, J., Karnieli, A., Herrmann, I., Królewicz, S. and Kuśnierek, K. 2010. Soil surface illumination at micro-relief scale and soil BRDF data collected by a hyperspectral camera. Int. J. Remote Sens. **31**: 2151–2157.

Coburn, C. A. and Noble, S. D. 2009. High performance field and laboratory goniometer for measuring hyperspectral bidirectional reflectance characteristics of various agricultural canopies. Proceedings of the 30th Canadian Symposium on Remote Sensing, Lethbridge, Alberta, Canada. Jun. 22–25.

Coburn, C. A. and Peddle, D. R. 2006. A low-cost field and laboratory goniometer system for estimating hyperspectral bidirectional reflectance. Can. J. Remote Sens. **32** (3): 244–253.

Croft, H., Anderson, K. and Kuhn, N. J. 2009. Characterizing soil surface roughness using a combined structural and spectral approach. Eur. J. Soil Sci. **60**: 431–442.

Garća Moreno, R., Díaz Álvarez, M. C., Tarquis, A. M., Paz González, A. and Saa Requejo, A. 2010. Shadow analysis of soil surface roughness compared to the chain set method and direct measurement of micro-relief. Biogeosci. Dis. **7**: 1021–1055.

Garća Moreno, R., Saa Requejo, A., Tarquis, A. M., Barrington, S. and Díaz Álvarez, M. C. 2008. A shadow analysis method to measure soil surface roughness. Geoderma **146**: 201–208.

Hapke, B., DiMucci, D., Nelson, R. and Smythe, W. 1996. The cause of the hot spot in vegetation canopies and soils: shadow-hiding versus coherent backscatter. Remote Sens. Environ. **58**: 63–68.

Huete, A. R. and Warrick, A. W. 1990. Assessment of vegetation and soil water regimes in partial canopies with optical remotely sensed data. Remote Sens. Environ. **32**: 155–167.

Irons, J., Campbell, G., Norman, J., Graham, D. and Kovalick, W. 1992. Prediction and measurement of soil bidirectional reflectance. IEEE Trans. Geosci. Remote Sens. **30**: 249–260.

Jackson, R. D., Teillet, P. M., Slater, P. N., Fedosejevs, G., Jasinski, M. F., Aase, J. K. and Moran, M. S. 1990. Bidirectional measurements of surface reflectance for view angle corrections of oblique imagery. Remote Sens. Environ. **32**: 189–202.

Jacquemoud, S., Baret, E. and Hanocq, J. F. 1992. Modeling spectral and bidirectional soil reflectance. Remote Sens. Environ. **41**: 123–132.

Ladoni, M., Alavipanah, S. K., Bahrami, H. A. and Noroozi, A. A. 2010. Remote sensing of soil organic carbon in semi-arid region of Iran. Arid Land Res. Manage. **24** (4): 271–281.

Lyapustin, A. I. and Privette, J. L. 1999. A new method of retrieving surface bidirectional reflectance from ground measurements: Atmospheric sensitivity study. J. Geophys. Res.-Atmos **104**: 6257–6268.

Ni, W. and Li, X. 2000. A coupled vegetation–soil bidirectional reflectance model for a semiarid landscape. Remote Sens. Environ. **74**: 113–124.

Nicodemus, F. E., Richmond, J. C., Hsia, J. J., Ginsberg, I. W. and Limperis, T. 1977. Geometrical considerations and nomenclature for reflectance. National Bureau of Standards Monograph, 160.

Oh, Y. and Kay, Y. C. 1998. Condition for precise measurement of soil surface roughness. IEEE Trans. Geosci. Remote Sens. **36**: 691–695.

Oh, Y., Sarabandi, K. and Ulaby, F. T. 1992. An empirical model and an inversion technique for radar scattering from bare soil surface. IEEE Trans. Geosci. Remote Sens. **30**: 370–382.

Peltoniemi, J. I., Kaasalainen, S., Näränen, J., Rautiainen, M., Stenberg, P., Smolander, H., Smolander, S. and Voipio, P. 2005. BRDF measurement of understory vegetation in pine forests: dwarf shrubs, lichen, and moss. Remote Sens. Environ. **94**: 343–354.

Richter, N., Chabrillat, S. and Kaufmann, H. 2005. Preliminary analysis for soil organic carbon determination from spectral reflectance in the frame of the EU project DeSurvey. Pages 96–101 *in* Proceedings of the 1st International Conference on Remote Sensing and Geoinformation Processing in the Assessment of Land Degradation and Desertification (RGLDD), Trier.

Sandmeier, S. and Itten, K. 1999. A field goniometer system (FIGOS) for acquisition of hyperspectral BRDF data. IEEE Trans. Geosci. Remote Sens. **37**: 648–658.

Sandmeier, S. R. and Strahler, A. H. 2000. BRDF laboratory measurements. Remote Sens. Rev. **18**: 481–502.

Schaepman-Strub, G., Schaepman, M., Dangel, S., Painter, T. and Martonchik, J. 2005. About the use of reflectance terminology in imaging spectroscopy. EARSeL eProceedings 4, **2**: 191–202.

Schmugge, T. and Jackson, T. J. 1994. Mapping surface soil moisture with microwave radiometers. Meteorol. Atmos. Phys. **54**: 213–223.

Schmugge, T. J., Gloersen, P., Wilheit, T. and Geiger, F. 1974. Remote sensing of soil moisture with microwave radiometers. J. Geophys. Res. **19**: 317–323.

Selige, T. and Schmidhalter, U. 2001. Remote sensing of soil properties to support site specific farming. Pages 878–879. *in* W. J. Horst et al., eds. Plant nutrition – Food security and sustainability of agro-ecosystems. Kluwer Academic Publishers, Dordrecht, the Netherlands.

Snyder, W. C. 2002. Definition and invariance properties of structured surface BRDF. IEEE Trans. Geosci. Remote Sens. **40**: 1032–1037.

Strub, G., Beisl, U., Schaepman, M., Schlaepfer, D., Dickerhof, C. and Itten, K. 2002. Evaluation of diurnal hyperspectral HDRF data acquired with the RSL field goniometer during the DAISEX'99 campaign. ISPRS J. Photo. Remote Sens. **57**: 184–193.

Suits, G. W. 1972. The calculation of the directional reflectance of a vegetative canopy. Remote Sens. Environ. **2**: 117–125.